Title

DDX6 Regulates the Assembly, Size and Fluidity of FUS Condensates

Authors

Mekonnen, Gemechu

Rhine, Kevin

Yuan, Xincheng

et al.

Publication Date

2025-02-13

DDX6 regulates the assembly, size and fluidity of FUS condensates

Gemechu Mekonnen[1,2,3,6], Kevin Rhine[2,3,6,*], Xincheng Yuan[1,2,3], Yingda Ge[1,4,5], Sophie Skanchy[4], Nilimesh Das[1], Sushil Pangeni[1,4,5], Tapas Paul[1], Sua Myong[1,2,3,5,7]

[1] Program in Cellular & Molecular Medicine, Boston Children's Hospital, Boston, MA 02115, USA.
[2] Program in Cell, Molecular, Developmental Biology, and Biophysics, Johns Hopkins University, Baltimore, MD 21218, USA.
[3] Department of Biology, Johns Hopkins University, Baltimore, MD 21218, USA.
[4] Department of Biophysics, Johns Hopkins University, Baltimore, MD 21218, USA
[5] Jenkins Biophysics Program, Johns Hopkins University, Baltimore, MD 21218, USA.
[6] Co-First Authors
[7] Corresponding Author, Email Address: sua.myong@childrens.harvard.edu
* Current Address: Department of Cellular & Molecular Medicine, University of California San Diego School of Medicine, La Jolla, CA 92037, USA.

Summary

FUS is a highly disordered RNA binding protein that readily undergoes phase separation. Mutations in FUS have been implicated in neurodegenerative diseases where mislocalized FUS facilitates the formation of aberrant RNP granules that aggregate in the cytoplasm. Still, the key molecular interactions which tune the assembly, size, and fluidity of FUS-containing granules remain unclear. Through an RNAi-based knockdown screen, we identified an RNA helicase, DDX6, which tunes FUS-positive stress granule (FUS-SG) formation in neuroblastoma cells. DDX6 plays a dual role in regulating FUS condensation by promoting the assembly of nano and meso-scale FUS clusters while limiting the size of micron-scale FUS droplets as a function of concentration. Remarkably, we show that a single DDX6 molecule is sufficient to recruit and assemble FUS into a higher-order complexes. Upon FUS phase separation into liquid droplets, DDX6 increases interphase molecular exchange, thereby promoting their fluidity. Notably, DDX6 also forms a non-contiguous ring around FUS condensates, preventing coarsening and reducing the interfacial tension on the droplets. We propose that the regulatory activity of DDX6 we observe may contribute to the biogenesis and regulation of FUS containing RNP granules in cells.

Keywords: FUS, DDX6, RNA binding proteins, nanoclusters, phase separation, condensates

Highlights

- FUS-SG formation is regulated by DDX6 in neuroblastoma cells.
- DDX6 promotes higher-order assembly of FUS into nanoscale clusters.
- DDX6 acts as a surfactant to reduce the size and increase the fluidity of FUS condensates.
- Aberrant phase separation of FUS mutants is antagonized by DDX6.

eTOC Blurb

Mekonnen et al. demonstrate that DDX6 plays a dual role in promoting FUS phase separation and tuning FUS condensate size, fluidity, and fusion.

Introduction

Biomolecular condensates are membranelles organelles in cells that form via phase separation, a process driven by multivalent protein-protein and protein-nucleic acid interactions. These condensates involve many cellular activities, including the integrated stress response (ISR) and ribosomal RNA biogenesis [1-7]. Moreover, assembling membraneless organelles expedites rapid intracellular biomolecular organization and adaption to environmental changes[8-10]. Cellular condensates comprise hundreds of unique nucleic acids and proteins, but their biogenesis depends on the activity of a small subset of biomolecules described as scaffolds. In the cytoplasm, stress granule (SG) formation upon stress is driven by the scaffold protein G3BP1 and the core ribonucleoprotein (RNP) network it helps assemble[3, 11]. In the nucleus, the formation of nuclear speckles involved in mRNA processing is facilitated by the SR family of splicing factors, including SRSF1[12]. This implies that most of the proteins and nucleic acids present are client molecules that preferentially partition into these condensates. Still, these proteins are critical in determining these condensates' material and functional properties.

Apart from their role as scaffolds that drive assembly, proteins also control multiphase organization and activity of cellular condensates. In the *C. elegans* single-cell embryo, heterotypic protein-protein interactions regulate P granule condensates' asymmetric distribution. Interfacial clustering of the protein MEG-3 on PGL-3 condensates tunes their size, biophysical properties, and spatial arrangement [13-15]. Dysregulation of P-granule assymetry produces embryos with severe defects in anterior-posterior organization. In the nucleolus, concentric, condensed protein layers direct the synthesis and maturation of ribosomal RNA (rRNA) [8, 16]. This is partially regulated by DDX21, which localizes to the interfacial boundary between the fibrillar center and dense fibrillar component and promotes the fluidity of RNA Pol I condensates [17, 18]. Thus, intermolecular interaction networks of scaffolds and clients drive multiphase condensate assembly and proper cellular function.

Fused in sarcoma (FUS) is a nuclear RNA binding protein (RBP) that regulates transcription, splicing, and trafficking of RNA [19-23]. Through its role in RNA processing, FUS can accumulate in the cytoplasm but is shuttled back to the nucleus by its cognate importin, Karyopherin-β2[24]. Mutations in *FUS* affecting its nuclear localization, RNA binding, and phase separation propensity are implicated in particularly severe forms of familial amyotrophic lateral sclerosis (ALS) and frontotemporal lobar dementia (FTLD) [25-28]. Notably, it contributes to the formation of insoluble cytoplasmic aggregates found in the motor neurons of ALS patients [29-34]. Upon stress, cytoplasmic mutant FUS is a client protein that preferentially partitions in SGs, increasing their size and abundance while significantly reshaping the biomolecular composition of the condensates [35, 36]. As a result of its prolonged mislocalization, FUS likely participates in *de novo* molecular interactions, which may drive its involvement in cell homeostasis, pathologies, and disease progression in neurodegeneration[37-41]. In this work, we aim to identify and explore what possible molecular interactions regulate the formation of these FUS-positive stress granules (FUS-SGs).

To identify proteins involved in enhancing or inhibiting FUS-SGs, we performed an RNAi-based reverse genetic screening targeting proteins known as FUS-interacting proteins and those commonly found in SGs. These include the FET (FUS, EWSR, and TAF15) proteins, RNA helicases involved in RNA processing and translation, and ALS-associated proteins such as TDP-43. We found that DDX6, an RNA helicase involved in both P-body (PB) and SG biogenesis, plays a dual role by promoting FUS-SG assembly and tuning, number, size, and total production of FUS-SGs under oxidative stress in a concentration dependent manner. Furthermore, our in vitro FUS phase separation assays showed that DDX6 controls FUS phase separation through four mechanisms: (1) promoting FUS assembly into nanoclusters at low FUS concentration, (2) decreasing the size of FUS condensates at high FUS concentration, (3) increasing the molecular exchange of FUS between the dense and dilute phase, and (4) reducing surface tension by forming interfacial clusters on FUS condensates. Together, our data demonstrate that DDX6 is a crucial protein regulating the assembly and physical properties of FUS condensates.

Materials and Methods

SH-SY5Y Cell Culture

Human SH-SY5Y neuroblastoma cells (ATCC #CRL-2266) were cultured in DMEM (Thermo #11960044) supplemented with 10% fetal bovine serum(NEB Catalog # B9000), 2 mM glutamate (Fisher #25030081), 0.15% (v/v) sodium bicarbonate (Fisher #25080094), and 1 mM sodium pyruvate (Thermo #11360070). Cells were incubated at 37 °C with 5% CO_2, and the media was changed every 96 h. SH-SY5Y cells were passaged using trypsin solution (Thermo #2530062) at a 1:10 split ratio. Frozen stocks were produced by resuspending cell pellets in 95% (v/v) fetal bovine serum with 5% (v/v) DMSO (Invitrogen # D12345).

The stable FUS-Halo cell line was generated by co-transfecting parental SH-SY5Y cell lines with pFUS-Halo[19] and the piggybac transposase (SBI #PB210PA-1) plasmids using Lipofectamine 3000 (Thermo #L3000008). Following 48 h incubation, the stably transfected cells were selected by treating with 200 µg/mL geneticin (Thermo #10131027), which was sufficient to kill non-transfected cells. Selection continued for at least 2 weeks before performing experiments with the FUS-Halo cells.

Immunofluorescence

FUS-Halo cells were passaged onto Nunc Lab-Tek II 4-well chambers (Thermo #154526) that were pre-coated with 5 µg/mL fibronectin. After 24 h incubation, the cells were washed three times with 1X dPBS (Thermo, #14190144) and fixed with 4% (v/v) paraformaldehyde (fisher, #AAJ19943K2) for 15 min at 25 °C. The samples were washed three times with 1X dPBS and were then permeabilized with 1X dPBS supplemented with 0.3% (v/v) Triton-X100 (millipore sigma, #9036-19-5) and 1% (w/v) bovine serum albumin (BSA; NEB Catalog # B9000) for 15 min at 25 °C. Following another set of three 1X dPBS washes, the primary antibodies (Table S2) were diluted in permeabilization solution and incubated for 16 h at 4 °C with gentle rocking. The cells were rewashed with 1X dPBS and treated with secondary antibodies for 1 h at 25 °C. After incubation with the secondary antibodies, the samples were treated with 25 nM JF549 and 1 µg/mL Hoechst for 15 min, mounted with Prolong Gold (Thermo #P10144), and sealed for imaging. An LSM-800 fluorescence confocal microscope with an Airyscan detector was used for superresolution imaging of the immunofluorescence slides. Pre-processing of Airyscan images was performed by Zen Blue (Zeiss), and cell images were further analyzed using ImageJ.

siRNA Screen

Short interfering RNAs (siRNAs) for the 25 candidate knockdowns were synthesized by IDT (Table S1). Nunc 8-well chambers (Thermo #155361) were coated with 5 µg/mL fibronectin (Sigma #F1141-1MG) for at least 15 min. FUS-Halo cells were seeded onto the 8-well chambers at ~50% confluency 48 h prior to the experiment. Approximately 24 h before imaging, the cells were transfected with 10 nM siRNA using Lipofectamine 3000. The following treatments were added to the cells at the indicated times prior to imaging: 0.5 mM sodium arsenite (Sigma #S7400-100G) 1 h prior to imaging; 25 nM Janelia Fluor 549 (Promega #GA1110) 30 min prior to imaging; and 1 µg/mL Hoechst 33342 (Thermo #62249) 15 min prior to imaging. Cells were imaged in the 408 nm (Hoechst) and 550 nm (JF549) channels using an LSM-700 fluorescence confocal microscope with a 63x objective. FUS-positive granules were quantified using a custom Matlab script that we created previously [42]. In brief, this script identified granules through dynamic masking of high-intensity puncta in the FUS channel compared to the surrounding background signal. The nuclear mask was used to assign each FUS-positive granule to a nearby nucleus; if the granule was too far from the nearest nucleus or too large (i.e.,>10 μm^2) to be considered a bona fide granule, the puncta was discarded. The mapped puncta were used to calculate the number of granules per cell and the average area of the granules for each condition. These parameters were compared to the noncoding siRNA control condition using Welch's t-test.

Tuning DDX6 Abundance in Cells and Image Analysis

To tune cellular DDX6 concentration, we used DDX6 siRNA 13.3 (Table 1) and DDX6-eGFP (Genscript, Table1). DDX6 siRNA 13.3 was transformed as described above at the following concentrations: 5 nM, 7.5 nM, 10 nM,

15 nM, and 20 nM. Cells were grown in Nunc 8-well plates (Thermo #167064) as described above and labeled with rabbit anti-FUS and mouse anti-DDX6 primary antibodies. Cells were imaged using an LSM-980 microscope with an Airyscan detector. After image processing, images were analyzed using CellProfiler™ cell image analysis software. Cells were first identified using Hoechst nuclear staining and the cell body using anti-FUS immunofluorescent staining. A mask was created to identify the cytoplasmic FUS signal by subtracting the nucleus primary object from the FUS cell body object. FUS-SGs were indentified using intensity thresholding parameters as described in the above section. Granules were assigned to cells based on the edges defined by the creation of the cell body object.

6xHis-MBP-FUS Purification

The expression construct of recombinant FUS fused to N-terminal 6xHis and maltose binding protein (MBP-FUS) was transformed into BL21 DE3 competent *E. coli* (Sigma #CMC0014-20X40UL). A TEV protease recognition sequence was inserted between the MBP and FUS open reading frames. FUS was purified as described previously [28]. In brief, a 5 mL starter culture was incubated in lysogeny broth (LB) with 50 µg/mL kanamycin sulfate (Millipore Sigma #70560-51-9) at 37 °C for 16 h at 200 rpm. The starter culture was used to inoculate 0.5 LB with kanamycin, which was then grown to an OD600 of ~0.4. MBP-FUS production was induced with 0.25 mM IPTG (Thermo Scientific #DF0446-17-3) at 30 °C for 2 h at 200 rpm. The cells were then pelleted, lysed for purification, filtered before loading, and passed through a 5 mL HisTrap HP column (Cytiva #17528601) using an ÄKTA Pure 25 M FPLC system (Cytiva). The bound protein was eluted with an increasing imidazole gradient and stored in 25% (v/v) glycerol at 4 °C for up to 2 weeks. Untagged FUS was purified by incubating the FUS-MBP from above with acTEV protease (Thermo #12575015; 1 µL acTEV to 10 nmol MBP-FUS) for 8 hours in a buffer containing 1 µM KCl and 1 µM Urea. The solution was then put back through the His-Trap column, and the flowthrough fractions containing untagged FUS were collected.

6xHis-MBP-DDX6 Purification

DDX6 was fused to a 6xHis and MBP tag at the N-terminal end of the protein. The expression construct was transformed into BL21 *E. coli*, which were then used to inoculate a 5 mL LB with a kanamycin starter culture. After incubating at 37 °C for 16 h at 200 rpm, the starter culture was used to inoculate 1 L LB with kanamycin. The 1 L culture was grown at 37 °C to an OD of ~0.8. DDX6 expression was then induced with 0.25 mM IPTG, and the culture was incubated at 30 °C for 2 h at 200 rpm. After protein induction, the cells were pelleted at 5000 x *g* for 10 min at 4 °C and either used immediately or stored at -80 °C.

Cell pellets were resuspended in DDX6 Lysis Buffer (50 mM Na_2HPO_4, 150 mM NaCl, 10 mM imidazole, 5 mM β-mercaptoethanol, 10 mg/L lysate RNase A, one-half-tablet complete protease inhibitor cocktail, 20 mM $MgSO_4$, 1% (v/v) IGEPAL CA-630, adjusted to pH 7.4) and sonicated at 20% amplitude for 6 min (8 s on/8 s off cycles). The lysate was centrifuged at 23644 x *g* for 30 min at 4 °C. The supernatant fraction was filtered through a 0.22 µm filter and loaded onto an ÄKTA Pure 25 M FPLC system. The lysate was passed through a 5 mL HisTrap HP column that was equilibrated and washed with DDX6 Binding Buffer (50 mM Na_2HPO_4, 150 mM NaCl, 10 mM imidazole, 5 mM β-mercaptoethanol, adjusted to pH 7.4). Crude DDX6 protein was eluted by steadily increasing the fraction of DDX6 Elution Buffer (50 mM Na_2HPO_4, 150 mM NaCl, 500 mM imidazole, 5 mM β-mercaptoethanol, adjusted to pH 7.4) and collecting fractions. The DDX6-containing fractions were detected by absorbance and SDS-PAGE, pooled together, and concentrated to <2 mL using a 50 mL Amicon filter (Sigma #UFC905008). The concentrated crude DDX6 was then loaded onto a Superdex 10/200 25 mL SEC column (Cytiva #28990944) that was equilibrated with DDX6 SEC Buffer (50 mM Na_2HPO_4, 150 mM NaCl, 5 mM β-mercaptoethanol, adjusted to pH 7.4). SEC fractions were analyzed for SDS-PAGE, and pure fractions containing DDX6 were pooled and concentrated. Glycerol was added to a final concentration of 10% (v/v), and DDX6 aliquots were flash-frozen in liquid nitrogen for long-term storage at -80 °C.

Electrophoresis mobility shift assay (EMSA)

EMSA was performed with purified DDX6-MBP. 1 nM of Cy5-NHS labeled U_{40} and SON RNAs were incubated with DDX6 in a buffer containing 50 mM Tris pH 7.4, 2 mM $MgCl_2$, 100 mM β-Mercaptoethanol, 0.1 mg/mL BSA,

and 100 mM KCl. After a 30-minute incubation at room temperature, samples were run on a 6% (w/v) acrylamide retardation non-denaturing gel at 150 V for 45 minutes. Gels were then imaged on a Typhoon 8100 with the cy5 channel.

Fluorescent Protein Labeling

FUS and DDX6 protein was labeled with Cy3 NHS ester (Cytiva #PA13101) and Cy5-NHS ester (Cytiva #PA15100) as described and validated previously[19, 42]. In brief, proteins were desalted with 0.5 mL Zeba Spin Desalting Columns (Thermo Scientific #89883) in a PBS-containing buffer following the manufacturer's protocol. The proteins were reacted with 4-5-fold-molar excess of fluorescent NHS ester for 45 min at 25 °C in the dark with rotation in 100 mM sodium bicarbonate. Excess dye was desalted with additional Zeba Spin Desalting Columns, and the dye conjugation efficiency was determined using a Nanodrop spectrophotometer. Labeled protein was stored at 4 °C in the dark for 2 weeks.

Single-molecule pulldown (SiMPull) assay

Single-molecule Analysis of FUS and DDX6 intermolecular interaction was performed using prism-based total internal reflection fluorescence microscopy as described [43, 44]. FUS and DDX6 were labeled with Cy3 and Cy5 using NHS-ester chemistry. First, the biotin-conjugated anti-MBP antibody was immobilized on a Polyethylene glycol (PEG) passivated slide surface through biotin- NeutrAvidin interaction. Then, MBP-tagged either FUS or DDX6 was added to the immobilized antibody-coated surface, followed by corresponding untagged (without MBP) DDX6 or FUS applied. The experiment was conducted at 10 mM Tris-HCl, pH-7.5, and 100 mM NaCl with an imaging buffer at room temperature [44].

Fluorescence correlation spectroscopy (FCS)

FCS was performed on a confocal C-Trap™ (Lumicks) instrument. FUS was labeled with Cy3 respectively using NHS-ester chemistry as described above and added to reactions at a final concentration of 20 nM. Cy3 labeled FUS, unlabeled FUS, and DDX6-MBP reactions were prepared in 1X cleavage buffer (100 mM NaCl, 50 mM Tris pH 7.4, 1 mM DTT, and 1 mM EDTA pH 8.0) with acTEV protease in a 50 µl. Reactions were incubated at room temperature for one hour. Fluorescence intensity measurements in the confocal volume were detected using ultra-low light detection and single photon counting. Sample intensity measurements were taken for 10 minutes and processed using an in-house Python script, which performed autocorrelation analysis.

Dynamic Light Scatter (DLS)

Dynamic light scattering experiments were performed using the Dynapro® Plate reader II (Wyatt Technology) with fixed angle light scattering. 100 µl sample reactions were prepared in 1X cleavage buffer (100 mM NaCl, 50 mM Tris pH 7.4, 1 mM DTT, and 1 mM EDTA pH 8.0) and deposited in a black Corning® 96 well plate (ref # 3881) for data collection. Measurements were performed using an 800 nm excitation laser at 25°C with an acquisition time of 5 seconds and 8 acquisitions taken per measurement. 50 total measurements were collected for each sample prepared. Autocorrelation functions, diffusion rates, and hydrodynamic radii of measured particles are collected and processed using Dynamics software (version 7.10.1.21,Waters™|Wyatt Technology) and analyzed using Microsoft Excel.

In Vitro Phase Separation Reactions

Phase separation reactions were performed essentially as described previously[19]. In brief, FUS was buffer-exchanged into 20 mM Na_3PO_4 using successive spins in Amicon filters (Sigma #UFC503008). FUS and DDX6 were combined with 10 U AcTEV protease (Thermo #12575015) in 1X Cleavage Buffer (100 mM NaCl, 50 mM Tris pH 7.4, 1 mM DTT, and 1 mM EDTA pH 8.0) and incubated in 8-well Nunc chambers for up to 6 h. The surface of the chamber was imaged using a Nikon Ti Eclipse wide-field microscope in the brightfield, 488 nm, 555 nm, and 637 nm channels. Videos were recorded using the same acquisition settings but for set intervals over time with definite focus enabled. Superresolution imaging was performed on an LSM-800 fluorescence confocal microscope. Phase separation images were processed using a custom Matlab script that masks each

droplet as a region of interest (ROI) and calculate statistics (e.g., number, area, total area coverage, etc.) en masse [42].

Fluorescence Recovery After Photobleaching (FRAP)

Whole or partial droplet FRAP experiments were conducted with a 50 mW 405 nm bleaching laser and Bruker Galvano mirror scanner attached to a Nikon Ti Eclipse wide-field microscope. Movies were acquired in the Alexa488, Cy3, or Cy5 channels, depending on the experiment. Movies were generally recorded for 10 min with acquisition every 3 s for 2 min then every 10 s for the remaining time. FRAP experiments were analyzed as described previously [28]. In brief, we corrected for stage drift and loss of intensity throughout the video using background and reference ROIs. The intensity of bleached droplets was then calculated relative to the background intensity over time.

Optical trap-directed droplet fusion

Controlled droplet fusions were performed essentially as described previously[45]. Large-scale (1 mL) phase separation reactions were performed as described above (see *In Vitro Phase Separation Reactions*). The droplets were flowed in a C-Trap Optical Tweezers (Lumicks) instrument. Two droplets were trapped with two of the optical tweezers, which were then moved into a separate flow channel with 1X Fusion Buffer (1X Cleavage Buffer with 10 mM Trolox, abcam # 53188-07-1). One trap was slowly moved in close proximity to another trap to allow spontaneous fusion and relaxation. Brightfield videos of each fusion event were recorded and analyzed as described previously by a custom Matlab script that determined the droplet aspect ratio over time to determine the viscoelastic properties of each droplet[45, 46].

Protein-ssDNA binding assays

Protein-ssDNA binding experiments were performed using optical tweezers combined with confocal microscopy (C-trap) from Lumicks B.V. Long single stranded DNA (48.5 knt) were formed by force stretching lambda double stranded lambda DNA with biotins in the same strand. Experiments were performed as detailed in[citation]. For DDX6 experiments, DDX6 was incubated in the DDX6 channel for 5-10 s then imaged in the imaging channel with an imaging buffer. For FUS and DDX6 interaction experiments, DDX6 was incubated in a different channel; ssDNA with DDX6 bound was taken into a channel where FUS was present and imaged. This allows a spontaneous binding of FUS either to ssDNA or DDX6 directly.

Results

DDX6 knockdown inhibits FUS-positive SG formation

Mislocalization of FUS from the nucleus to the cytoplasm is a critical hallmark of ALS and FTLD. To model this mislocalization and to visualize FUS, we engineered an SH-SY5Y neuroblastoma cell line that stably expressed FUS with a C-terminal Halo tag. Because the nuclear localization signal (NLS) of FUS is at the extreme C-terminus of the protein, the Halo tag interferes with the nuclear import of FUS, resulting in some cytoplasmic localization of FUS [47, 48]. The exogenous FUS-Halo expression does not induce cytoplasmic FUS condensation under physiological conditions; FUS-SGs are only observed when acute stressors such as sodium arsenite are added to the cells. We applied Janelia fluor labels to measure FUS-SG formation and evaluated how FUS-interacting proteins impact FUS condensation in live cells.

Using previously published FUS datasets [37, 41, 49-52], we identified 25 proteins that likely impact FUS condensation in cells. Many are linked with neurodegeneration, known components in PBs and SGs, or other FUS regulators such as the importin Karyopherin-β2 (TNPO1). We treated FUS-Halo SH-SY5Y cells with siRNAs, which targeted transcripts coding for these 25 proteins for 24 hours, added Janelia Fluor 549 and Hoechst dye for visualization, and stressed the cells with 0.5 mM sodium arsenite for 30 min prior to live-cell imaging with a confocal fluorescence microscope (Figure 1A). The FUS signal was analyzed with a custom Matlab script which identified FUS-SG puncta in each cell [42]; this allowed us to calculate the number of granules per cell and the average area of these granules, both of which we used to determine whether these proteins impacted FUS condensation in SH-SY5Y cells.

Our screen identified two proteins which significantly decreased the size and number of FUS-SGs per cell: the RNA helicases DDX6 and DHX36 (Figure 1B-C). In addition to these helicases, several other knockdowns significantly decreased the average area of FUS-positive granules: TAF15, EWSR1, Ataxin2, HSBP1, and SFPQ (Figure 1B). The positive control – a FUS knockdown –significantly reduced granule formation (Figure 1B-C). Meanwhile, a scrambled siRNA did not impact FUS condensation (Figure 1B-C). Because the DDX6 knockdown condition had the most significant decrease in the number of FUS-SGs per cell and the average area of FUS-SGs, we focused on this protein for our studies. We further verified that siRNAs targeting different regions of the DDX6 mRNA had similar impacts on FUS-SGs (Figure S1B-D). FUS is known to interact with G3BP1 and Caprin1 within SGs, while DDX6 is found at low levels in SG but is enriched in PBs. To determine whether a physical association between DDX6 and FUS might underlie the regulation of FUS-SG condensation *in cellulo*, we performed Airyscan superresolution microscopy of fixed FUS-Halo cells. We found that FUS-Halo- and G3BP1-containing SGs are physically associated with DDX6- and Edc4-containing PBs (Figure 1D-E, S1A), which is consistent with other reports that have described PBs as points of assembly of new SGs and show that they remain tethered afterward [6, 53, 54].

DDX6 tunes FUS granule formation

The abundance of associated biomolecules in the environment can strongly impact a protein's phase separation propensity [55-57]. Our knockdown results reveal that DDX6 is required for FUS-SG formation. Therefore, we tested whether applying a gradient of DDX6 concentration via titration of siRNA knockdowns and exogenous overexpression constructs would also impact the number and size of FUS-SG condensates in SH-SY5Y cells. To this end, we transfected the FUS-Halo SH-SY5Y cell line with varying concentrations of a DDX6-targeting siRNA ([siRNA] = 5-20 nM) and a DDX6-GFP overexpression construct (DDX6-GFP = 0.1-2.0 μg). We verified that our transfections successfully modulated the DDX6 concentration in cells using a Western blot for endogenous and exogenous DDX6 expression (Figure S1E-H). The titrated cells were stressed with sodium arsenite, fixed with paraformaldehyde, and imaged for FUS-SG count and size, as performed for the screen

above (Figure 2A). We found that decreasing DDX6 concentration by increasing siRNA amount resulted in a gradual reduction in FUS-SG total area per cell, consistent with what we observed in our screen in Figure 1 (Figure 2B, Figure S1I-J). Surprisingly, overexpression of DDX6-GFP resulted in an unexpected pattern of change in FUS-SGs. We first observed that FUS-SGs increased in total area for plasmid transfection amounts of 0.1 – 1 μg (Figure 2C). However, this trend reversed when >1 μg DDX6-GFP was added: the FUS-SG total area decreased (Figure 2C). Therefore, while DDX6-GFP overexpression promoted overall FUS-SG condensation between 0.4-1.5 μg of plasmid transfection, the extent of FUS-SG formation decreased above 1.5 μg. Our results demonstrate that DDX6 protein levels dynamically regulate the FUS-SG formation in SH-SY5Y cells and indicate that DDX6 may buffer FUS-SG formation in the cell.

DDX6 promotes FUS cluster assembly

FUS and DDX6 share several relevant protein partners, including Atxn2 and UBQLN2, which impact SG formation [40, 58, 59]. It has been reported that DDX6 regulates SG biogenesis in cells [6, 60]; however, it is unclear if DDX6 can affect FUS-SG assembly through direct interactions with FUS. We used several orthogonal *in vitro* methods to test if DDX6 can interact with and regulate FUS condensation in a two-component system. We purified human FUS and DDX6 protein from *E. coli* (Figure S2A). Each overexpression construct was designed with an N-terminal MBP tag that antagonized native phase separation; cleavage of the MBP tag was initiated by adding TEV protease, which allowed phase separation under physiological salt conditions. For visualization, we fluorescently labeled and doped in 1% FUS and DDX6 with Cy3 and Cy5, respectively, which we previously showed does not impact FUS [42].

We first tested how DDX6 would affect FUS cluster assembly by employing dynamic light scattering (DLS) and fluorescence correlation spectroscopy (FCS), which are well suited to measure 1 nm-1 μm sized particles. We prepared untagged FUS (i.e., pre-cleaved FUS without the MBP solubility tag) to bypass the kinetic bottleneck of TEV protease-mediated MBP cleavage and to achieve rapid assembly. We first performed DLS measurements at a FUS concentration of 200 nM, significantly below the critical C_{sat} (~1 μM) for FUS droplet formation [28]. At this concentration, we found that FUS forms clusters of ~200-400 nm in diameter (Figure 3A). However, adding DDX6 at concentrations as low as 10 nM led FUS cluster sizes to increase by an order of magnitude, approaching 2-3 μm (Figure 3A). Higher concentrations of DDX6 (25 & 100 nM) also resulted in the detection of >3 μm particles (Figure 3B). We also imaged this assembly process, increasing sub-saturated concentrations of FUS in the presence of 100 nM DDX6, and found that cluster assembly was driven by DDX6 (Figure S3F). We then performed these same DLS measurements at 4 μM, well above its C_{sat}, which induced robust phase separation of FUS. Strikingly, we found that increasing concentrations of DDX6 strongly reduced the cluster size to 200 nm in diameter. Therefore, consistent with the cellular results, our DLS data demonstrates that DDX6 potently stimulates higher order FUS cluster assembly in a substoichiometric manner while limiting particle size at higher FUS concentrations.

Next, we performed FCS to test further the role of DDX6 on FUS assembly over a wide range of concentrations. At a sub-saturated concentration of 100 nM FUS (1% labeled with Cy3-FUS), the addition of DDX6 slowed the diffusion of FUS clusters by half, indicating an increase in size (Figure 3F). For higher concentrations of FUS (500 nM), we observed an intriguing pattern of an increase followed by a decrease in FUS cluster size as a function of DDX6 concentration, which is reminiscent of the cellular data, which also demonstrated a rise followed by a fall in FUS-SG size as a function of increasing DDX6 transfection (Figure 3G, Figure S1I). At a FUS concentration of 1 μM that exceeds its C_{sat}, the same range of DDX6 concentrations significantly increased the diffusion, i.e., it decreased the size of FUS clusters by an order of magnitude(Figure 3H). The result indicates that DDX6 may tune FUS phase separation by promoting assembly at sub-C_{sat} and reducing the condensate size above its C_{sat}, which mirrors FUS-SG regulation in cells (Figure 2).

DDX6 alone did not form visible condensates at physiological salt and DDX6 concentrations (Figure S2A); however, dextran and RNA did produce DDX6 aggregates at high concentrations (Figure S2B-E). In addition, dynamic light scattering (DLS) measurements revealed that DDX6 assembled nanoscale clusters that did not grow past 200 nm in diameter after 3 hours (Figure S2F).

DDX6 can recruit and nucleate FUS oligomers as a single molecule

DDX6 has several canonical binding partners, including LSM14A, 4E-T, and EDC3, that promote PB assembly and imply its role as a scaffold protein[61-64]. Our results demonstrate the promotion of FUS assembly at sub-saturated concentrations, supporting this claim. We performed single molecule pulldown (SiMPull) measurements on a total internal reflection fluorescence (TIRF) microscope to test this further. We immobilized MBP-tagged Cy5-DDX6 to our imaging surface coated with an anti-MBP antibody and flowed in Cy3-labeled FUS, untagged FUS (10 nM) (Figure 4A). We detected high Cy3/Cy5 colocalization levels, providing evidence of direct interaction between the two proteins at the level of single molecules (Figure 4B). Furthermore, we observed a gradual increase in Cy3-FUS intensity per Cy5-DDX6 spots over time, indicating that a single DDX6 molecule recruits multiple units of FUS(Figure 4C). Individual single-molecule traces at Cy5-DDX6-MBP foci revealed examples of nearly 10-fold increases in Cy3-FUS intensity after 300 s. We identified patterns in FUS assembly that follow both smooth (left) and uneven (right) increases over time(Figure 4C). We calculated the normalized mean intensity for colocalized Cy3-FUS intensity and discovered a linear increase as a function of time, indicating gradual accumulation of FUS at immobilized DDX6 foci(Figure S3D). Notably, the inverse arrangement of labelled DDX6 flowed over immobilized MBP-FUS produced only transient spikes in fluorescence intensity over time. Furthermore, labeled FUS applied to immobilized MBP-FUS showed no change in fluorescence, strengthening the specificity of FUS assembly dependent on DDX6 (Figure 4D-G & S3E).

To examine the potential FUS-DDX6 interaction in the context of nucleic acid, we next used dual-trap optical tweezers, C-TRAP (LUMICKS). We attached λ-ssDNA to the dual-trap beads and flowed in low nanomolar concentrations of FUS and DDX6 separately and sequentially. Cy3 FUS did not bind the ssDNA alone (Figure S3E). By contrast, Cy5-DDX6 bound and diffused on the DNA (Figure S3F). Remarkably, FUS oligomers engaged with DDX6 and co-diffused along the ssDNA (Figure S3C). These results indicate that DDX6 could recruit FUS multimers to ssDNA, confirming its ability to interact with and nucleate FUS assemblies.

In summary, we demonstrate that DDX6 and FUS physically interact and, importantly, that DDX6 can recruite and induce higher-order assembly of FUS into nanoscale clusters. Our experiments demonstrate several key findings: (1) FUS and DDX6 directly interact; (2) DDX6, even at the single molecule level, promotes the nucleation of FUS clusters, and (3) DDX6 may buffer the over-growth of micron-scale FUS condensates.

DDX6 tunes FUS condensate size by forming interfacial clusters

Given that DDX6 can modulate the assembly of sub-micron-sized FUS clusters, we asked how DDX6 may regulate the physical properties of micron-scale phase separated FUS droplets by imaging. (Figure 5A). We added DDX6 protein (0.1-4 μM) to 4 μM FUS and observed that 0.1-1 μM DDX6 (1:40 to 1:4 DDX6:FUS) reduced FUS condensate area while concomitantly increasing the number of condensates over twofold (Figure 5C-D). This anti-correlated pattern between the condensate area versus count slightly reversed at higher DDX6 concentrations but reflected directional inhibition of FUS condensation as shown by a quantification of droplet total area (Figure 5E). This agrees with DLS measurements, which showed that DDX6 inhibits FUS phase separation by buffering the assembly of FUS into phase separated > 1 μm droplets at high concentrations (Figure 3B). Importantly, this dynamic change in FUS droplet size and count aligns with the outcomes on FUS-SG size

we observed in SH-SY5Y cells (Figure 2, Figure S1I-J). Together, this result further demonstrates the role of DDX6 in tuning the size of the FUS condensates *in vitro* and FUS-positive granules in cells.

Interestingly, Cy5-DDX6 formed a distinct ring-like pattern around FUS condensates (Figure 5B). This phenomenon was observed from low, substoichiometric DDX6 concentrations (i.e., 160-fold less DDX6 than FUS) up to equimolar FUS and DDX6 concentrations, indicating that the ring-like structure is an inherent concentration-independent pattern. Superresolution Airyscan imaging revealed that DDX6 is mostly depleted from the internal FUS-containing condensate and consists of small puncta within the ring-like structures attached to the FUS condensates (Figure 5B), which resembles the pattern of DDX6 containing P-bodies juxtaposed at the periphery of FUS-SGs in cells (Figure 2A) Furthermore, we found that these puncta diffused along the surface of the FUS condensates (Video S1). This ring-like morphology is reminiscent of interfacial clusters observed by others [15, 55, 65-68].

DDX6 interfacial clusters alter the material properties of FUS condensates

Next, we asked if DDX6 also altered the surface properties of the condensates. FUS droplets that would otherwise fuse upon contact and wet the imaging surface persisted as attached couplets and were organized in chains and bunches in the presence of DDX6 (Figure S4A). To further explore this, we performed controlled fusion experiments of FUS droplets with and without DDX6 using dual-laser optical tweezers, C-TRAP [45]. We found that FUS-DDX6 condensates are highly resistant to fusion; we collected and plotted the fusion data from droplets of varying sizes over time and extracted a slope that represents the inverse capillary velocity, viscosity(η) divided by surface tension (γ). A marked increase in the η/γ slope for FUS-DDX6 droplets signifies that DDX6 reduced the surface tension acting on the droplets, resisting fusion (Figure 5F-G). These data suggest that DDX6 forms interfacial clusters around FUS condensates that inhibit coalescence, thereby regulating the condensate size. We show that a nonspecific protein, BSA, cannot recapitulate the effect of DDX6 on FUS, further strengthening the specific role of DDX6 on FUS (Figure S4D).

In a previously reported case of interfacial clusters, it was stated that the surfactants reduced the coarsening of condensates while increasing the exchange of the scaffold protein between the two phases[15]. To test whether DDX6 exerted a similar effect on FUS, we performed fluorescence recovery after photobleaching (FRAP) of FUS condensates with and without DDX6. Consistent with the previous findings, we observed that DDX6 significantly increased FUS fluidity by increasing the interphase exchange of FUS between the dense and dilute phases(Figure 5H-I). By contrast, the DDX6 clusters were largely immobile, failing to exchange with other DDX6 proteins inside the ring or with free DDX6 in solution (Figure 5J). The outer shell-like property exhibited by DDX6 also agrees with the previous interfacial clusters formed by MEG-3 in *C. elegans* [15].

DDX6 regulates the size and fluidity of RNA-FUS co-condensates

DDX6 and FUS are both RBPs. In the cell, they are in RNA-rich environments where RNA can promote nucleation or buffer phase separation of the RBPs depending on the relative concentrations. To test the effect of RNA in vitro, we used the U_{40} homopolymer, an unstructured RNA frequently employed to promote phase separation. Our phase separation experiments showed the same FUS-DDX6 core-ring architecture and U_{40} localized to the core of the FUS condensates. We further confirmed that switching the Cy3/Cy5 labeling of FUS and DDX6 did not affect the localization of any of the three components (Figure S5A-B).

Similar to FUS-DDX6 condensates, we also observed that FUS-RNA-DDX6 condensates changed in average area and count as a function of DDX6 concentration in a very similar manner to our FUS-DDX6 experiments in Figure 5 but to a lesser magnitude (Figure 6A-C). Likewise, the total area coverage of the RNA-containing

condensates showed a similar decrease to approximately half of the initial area when the highest DDX6 concentration was applied (Figure 6D). DDX6 also increased the FRAP recovery of U_{40} and FUS, reflecting the increased exchange of FUS and RNA between the dense and dilute phases in the presence of DDX6 (Figure 6E-G). Nevertheless, the impact of DDX6 on FUS exchange was less than the condition without the RNA. From these findings, we conclude that DDX6 regulation of FUS condensation is similar but slightly attenuated by the presence of RNA, and DDX6 can increase the interphase mobility of both FUS and RNA in the tripartite condensates. Measurement of FUS droplet size and number with structured SON RNA displayed a similar impact as the unstructured U_{40} (Figure S5C-F). Finally, we found that the DDX6 regulation of FUS condensates is ATPase independent by performing our droplet assays with ATP, Mg^{2+}, and a DQAD mutant of DDX6, which cannot hydrolyze ATP. Adding ATP and magnesium at physiological concentrations with $DDX6^{WT}$ produced a mild reduction in droplet formation. Experiments with $DDX6^{DQAD}$ produced similar, albeit diminished, effects on droplet area and count (Figure S5G-H & S6).

DDX6 antagonizes phase separation of ALS-linked FUS variants

DDX6 effectively diminishes FUS^{R244C} and, to a lesser extent, FUS^{G156E} droplet size (Figure 7A-B). For FUS^{R244C}, regulation of droplet area was much more prominent than droplet count (Figure 7C-D). The effect of DDX6 on the FUS^{R244C} droplet area was quite dramatic: FUS^{WT} droplet area fell with the addition of 100 nM DDX6; in contrast, the FUS^{R244C} area fell by more than 2-fold difference in effect compared to FUS^{WT} (Figure 7D-E). However, The droplet count only increased by 20%, resulting in a decrease in total area of FUS^{R244C} droplets (Figure 7E). Overall, regulation of FUS^{R244C} condensates is underscored by the near-complete loss of large and non-circular condensates when 1 μM DDX6 is added (Figure 7G-H). Given that large and irregularly shaped condensates are a signature of pathogenic phase separation of FUS^{R244C} *in vitro* [28], our data suggests that DDX6 may directly antagonize disease-associated maturation of FUS mutants.

Unlike FUS^{WT} and FUS^{R244C}, we found that FUS^{G156E} droplet count did not have a discernible trend but decreased FUS^{G156E} droplet area as a function of DDX6 concentration (Figure 7E). Consequently, DDX6 exerts a mild effect on the total area covered by FUS^{G156E} condensates (Figure 7F). This is likely because FUS^{G156E} condensates are gel-like and small [19]. Furthermore, we tested how DDX6 affected FUS^{G156E} fluidity. We found that adding equimolar DDX6 leads to a notable increase in both FUS^{R244C} and FUS^{G156E} FRAP (Figure 6I), indicating that DDX6 can increase the fluidity of this disease-associated mutant. In summary, DDX6 tunes the condensate size and material property of disease-associated FUS mutants.

Discussion

The diversity of protein-protein and protein-RNA interactions within the cell produces a multiphase emulsion of compositionally unique condensates. How these interactions regulate the formation and properties of cellular condensates remains largely unknown. In this work, we utilize *in cellulo* and *in vitro* methods to examine how DDX6, a key regulator of PB and SG formation, effectively regulates the assembly and material properties of FUS condensates (Figure 8).

We performed a targeted RNAi screen in SH-SY5Y cells to find genes that might regulate FUS condensation. We focused our search on proteins associated with FUS and core SG components (Figure 1). Our screen identified the protein DDX6 as a regulatory candidate, as its depletion reduced FUS-SG formation, and overexpression promoted the formation of larger granules to a point (Figure 2). Based on this finding, we hypothesized that DDX6 promoted FUS-SG assembly. A study of the literature provides no precise mechanism by which DDX6 might impact FUS-SG formation. However, its interaction with PB- and SG-associated proteins is important for proper cellular function.

DDX6 is an ATP-dependent RNA helicase required for miRNA-mediated transcription inhibition and decapping in PBs [69-71]. Thus, it is plausible that DDX6 regulates the formation of FUS-SG condensates by an ATP-dependent remodeling of RNA. However, in our *in vitro* droplet assay, DDX6 directly impacted FUS phase separation across a range of sub-stoichiometric concentrations, even without RNA or ATP (Figures 3 & 4). During the nucleation process, DDX6 promoted the formation of large clusters at FUS: DDX6 ratios as low as 40:1. In FUS droplet forming conditions, DDX6 formed interfacial clusters that increased FUS condensate fluidity, decelerated droplet coarsening, and antagonized spontaneous fusion events. Although this interfacial DDX6 produced little FRAP, real-time video recording of its movement on the surface revealed striking examples of rapid diffusion on the surface of FUS droplets. Together, these results suggest that DDX6 plays a dual role: it can drive FUS nanocluster assembly below its C_{sat} while constraining the size of condensates above the C_{sat}, possibly through its interfacial localization. Importantly, this DDX6-mediated regulatory activity can occur independently of RNA or ATP.

The ability of DDX6 to increase the rate of molecular exchange between the dense and dilute phases can be explained by several potential mechanisms. First, DDX6-induced FUS clusters may exhibit FUS-FUS interaction with a high association and dissociation rate, leading to more rapid recovery. Second, DDX6 may actively channel FUS in and out of the condensate, lowering the energetic barrier required to enter and exit the condensate. Third, DDX6 reduces the surface tension at the droplet-solvent interphase. Doing so may reduce the energy that FUS and RNA need to traverse this interfacial barrier[72]. Our results indicate that the third is most likely, given the apparent changes in surface tension measured by controlled droplet fusions measurements (Figure 5).

Several recent publications have reported that cells contain a stable pool of RNP nanoclusters at a concentration below the threshold required for phase separation[73-75]. This pool can act as a sensor that is activated by changes in cellular homeostasis, e.g., oxidative stress. Even at concentrations far surpassing what has been measured in cells, DDX6 does not undergo robust phase separate at a wide range of salt, pH, RNA, and cofactor concentrations [76](Figure S2A-F). However, our DLS measurements revealed that it can form nanoscale clusters on its own; in the cell, these nanoclusters may interact with other proteins and trigger their assembly into sub-micron RNP complexes that are precursors to condensates. These interactions likely occur through contacts made using the C-terminal RecA domain by which DDX6 binds its protein partners in the cell[61, 69, 71, 77]. It becomes clear that both self-assembly and heterotypic interactions with partner proteins play a critical role in defining the function of DDX6.

Even though DDX6 is an ATP-dependent RNA helicase, its ability to control FUS-RNA phase separation does not require ATP hydrolysis. RNA did not directly impact this function in our experiments, but it did accentuate the trends we observed in the FUS-DDX6 condensates. Nonetheless, the addition of ATP and Mg^{2+} likely enhances its regulatory capabilities. Others have reported that mutating the DEAD domain of DDX6 to DQAD disrupts its ability to tune the size and morphology of SGs within cells. Our in vitro droplet assays show that $DDX6^{DQAD}$ can still regulate FUS; however, its effect is attenuated. Interestingly, DDX6 exhibits an ATP-independent diffusion along single-stranded nucleic acids, and FUS can co-diffuse through the physical interaction with DDX6 (Figure S3C). In light of other reports that only observe weak ATPase activity by DDX6 [71], our ATPase-independent assays may also be relevant in cells. DDX6's activity in antagonizing the phase transitions of ALS-linked FUS variants introduces new avenues for applying this knowledge to therapeutic purposes as well.

Our multi-scale approach showed that DDX6 regulates protein condensates in cells and *in vitro*. In the cell, increasing DDX6 abundance leads to increases followed by decreases in total FUS-SG condensation. In our droplet experiments, DDX6 promoted FUS nanocluster assembly in low FUS concentration, while applying DDX6 caused a reduction in condensate size at high FUS concentration. Despite the complex milieu of the cell and the many other molecular interactions DDX6 and FUS participate in cells, the similarity between the in vitro and cellular observation suggests that the role of DDX6 may be dominant and prominent. Notably, the DDX6-

dependent effect may be cell or tissue-specific. We found that our in vitro results agree well with the cell-based observations found in Ripin et al., who showed that depletion of DDX6 in U2OS cells decreases SG formation. Interestingly, Majerciak et al. recently showed that the deletion of DDX6 in HeLa cells produced substantial PB-SG assembly defects. Furthermore, examining tissue-specific expression for DDX6 shows exceptionally high levels in the brain[78]. These findings and our own indicate strong cell type and likely even organism levlel specificity in the role of DDX6. This diversity likely depends on differing expression levels, DDX6 splice variants, and different protein and nucleic acid binding partners[79].

Biomolecular condensates and their existence as a multiphasic emulsion within the cell provide living systems with a dynamic method for cellular organization. Our findings here provide one mechanistic explanation of how the cell might regulate these condensates' size, abundance, and material properties. With further exploration of protein valency, RNA sequence composition and structure, and chaperone contribution, we believe a more complete model for biomolecular condensates' functional role in living systems and disease can be further illuminated.

Acknowledgments

We thank the Taekjip Ha and Sua Myong lab members for their technical and experimental assistance. We acknowledge funding support from the National Institutes of Health grants F31-GM148067 (GM), F31-NS113439 (KR), T32-GM007231 (GM and KR), RF1-AG071326 (SM), and RF1-NS113636 (SM), the National Science Foundation grant PHY-1430124 via the Center for Physics of Living Cells (SM), and the Johns Hopkins Discovery Award (SM).

Author Contributions

Conceptualization, GM, KR, and SM; Methodology, GM, KR, YG, SP, TP, ND, and SS; Investigation, GM, KR, YG, SP, TP, ND, XY, and SS; Formal Analysis: GM, KR, YG, SP, TP, ND, and SS; Writing – Original Draft, GM KR, and SM; Writing – Review & Editing, GM, KR, and SM; Funding Acquisition, GM, KR, and SM; Supervision, SM.

Declaration of Interests

Sua Myong is an advisory board member for *Molecular Cell*. The other authors declare no competing interests.

Figure 1

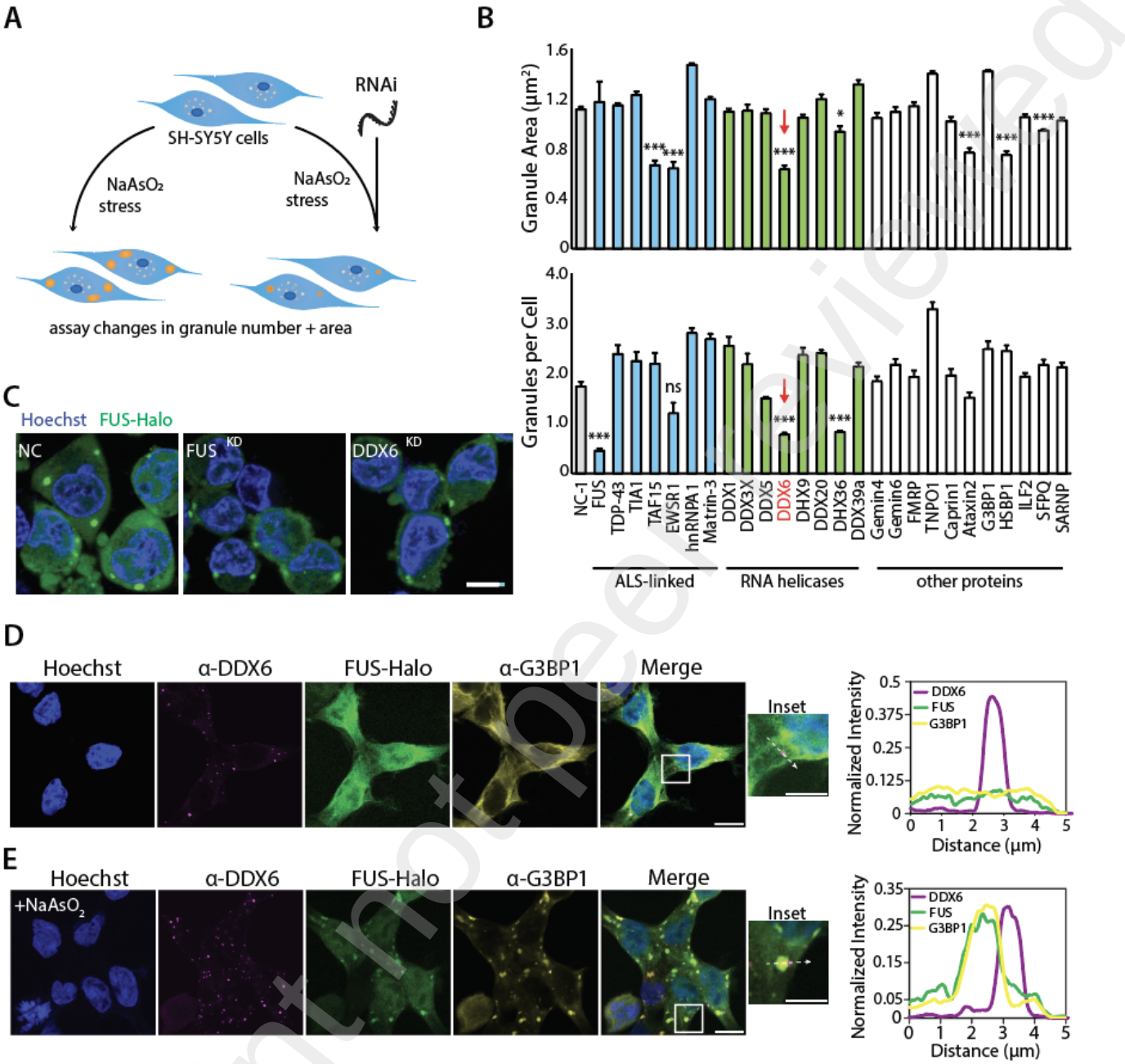

Figure 1: DDX6 drives FUS-SG formation in SH-SY5Y$^{FUS\text{-}Halo}$ cells. (A) Schematic of the reverse genetic screen to identify proteins that impact FUS-SG phase separation. **(B)** Quantification of the average FUS-SG area (top) and average FUS-SGs per cell (bottom) in SH-SY5Y$^{FUS\text{-}Halo}$ cells treated with the indicated sivRNAs and stressed with sodium arsenite. Error bars denote standard deviation. Statistics were calculated using a one-tailed Welch's t-test compared to the NC-1 (noncoding shRNA) control where ns = not significant and *** = p<0.001. Red arrow highlights DDX6. **(C)** Representative live-cell microscopy images of FUS-Halo (green) and Hoechst (blue) in SH-SY5Y$^{FUS\text{-}Halo}$ cells treated with the indicated siRNAs and sodium arsenite. Scale Bar = 10 μm. **(D)** Airyscan confocal immunofluorescence images of Hoechst (blue), DDX6 (magenta), FUS-Halo (green), and G3BP1 (yellow) in SH-SY5Y$^{FUS\text{-}Halo}$ cells. The white box denotes the inset, and the white-dashed line denotes the intensity profile plot. Scale Bar = 10 μm. **(E)** Same as (D) but for arsenite-treated cells.

Figure 2

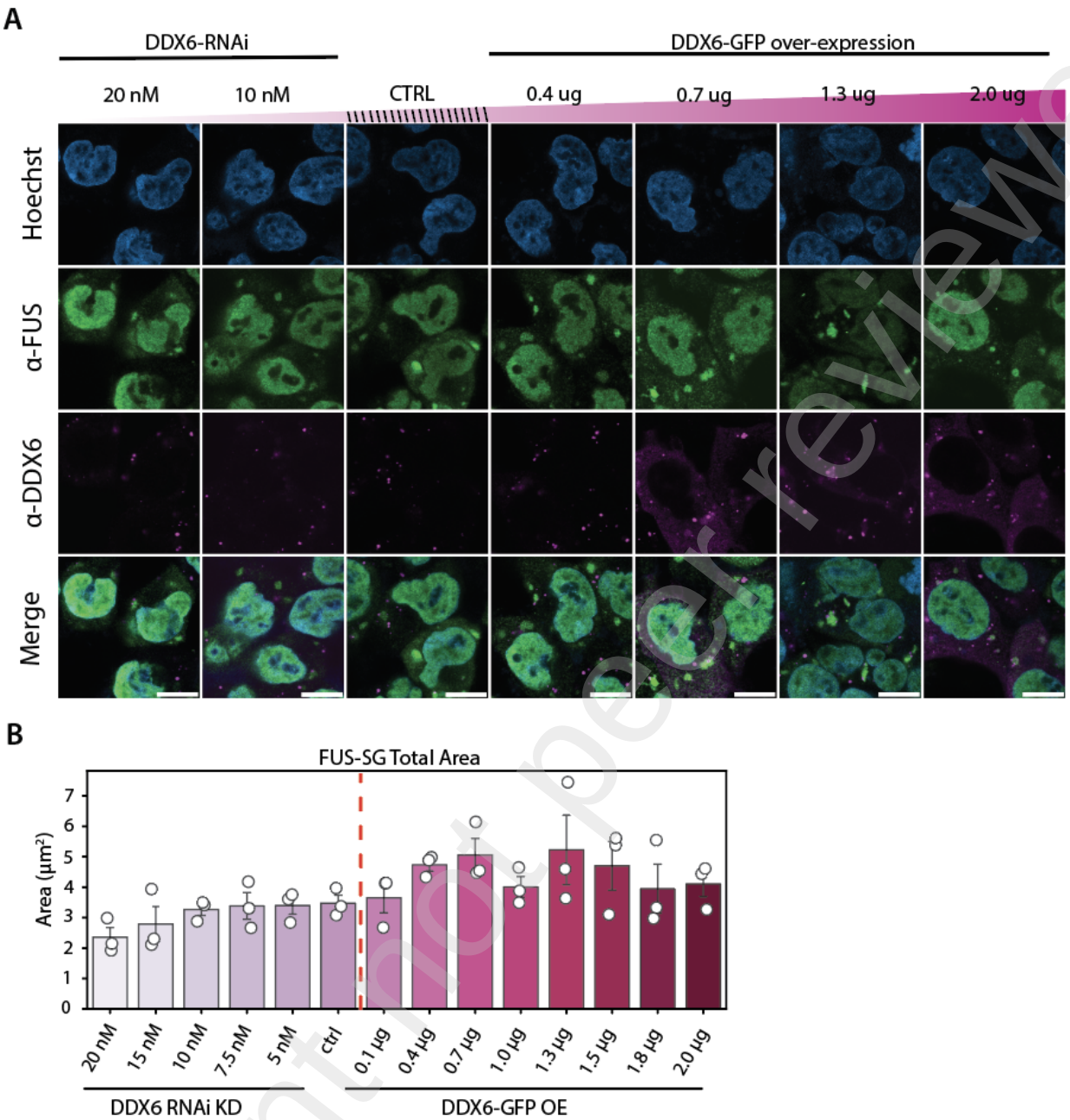

Figure 2: The intracellular abundance of DDX6 regulates FUS-SG phase separation. (A) Representative Airyscan confocal immunofluorescence images of Hoechst (blue), FUS (green), and DDX6 (magenta) in SH-SY5Y$^{FUS\text{-}Halo}$ cells treated with increasing amounts of DDX6-targeting siRNA (left) or increasing amounts of a DDX6-GFP overexpression construct. Scale Bar = 10 µm. **(B)** Quantification of average FUS-SG area for cells treated with increasing concentrations of DDX6-targeting shRNA or DDX6-GFP. Dots represent the mean of individual replicates. The error bars denote standard error across all replicates.

Figure 3

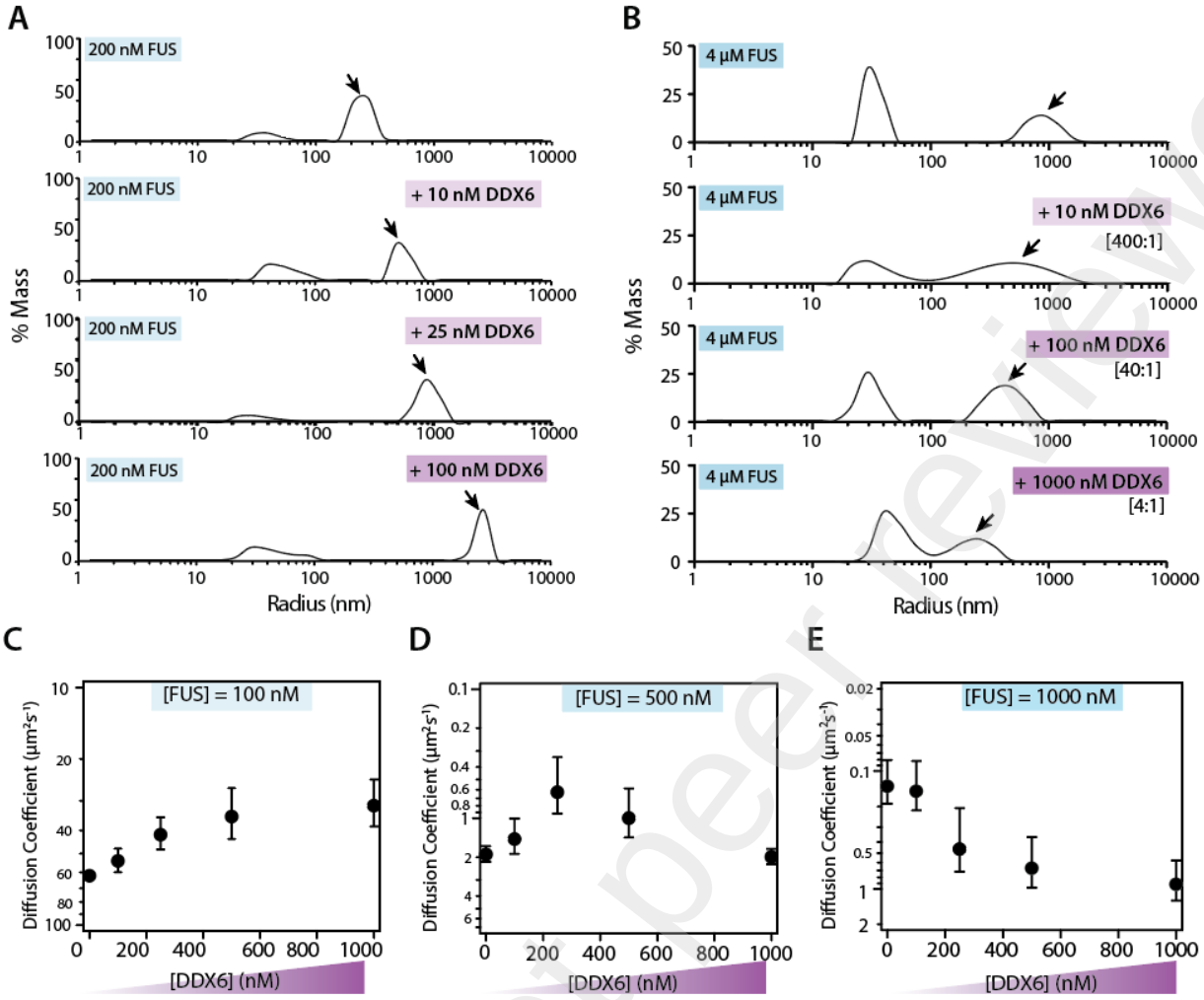

Figure 3: DDX6 dynamically regulates FUS cluster assembly and condensation. (A) DLS distribution of particle size as a function mass % for particles detected at a sub-saturated FUS concentration of 200 nM with increasing concentrations of DDX6. **(B)** Same as (A) for 4 µM FUS. **(C)** FCS measurement of the average FUS diffusion coefficient of 100 nM FUS with increasing concentrations of. Error bars denote standard deviation. **(D)** Same as (C) but with 500 nM FUS. **(E)** Same as (C) but with 1000 nM FUS.

Figure 4

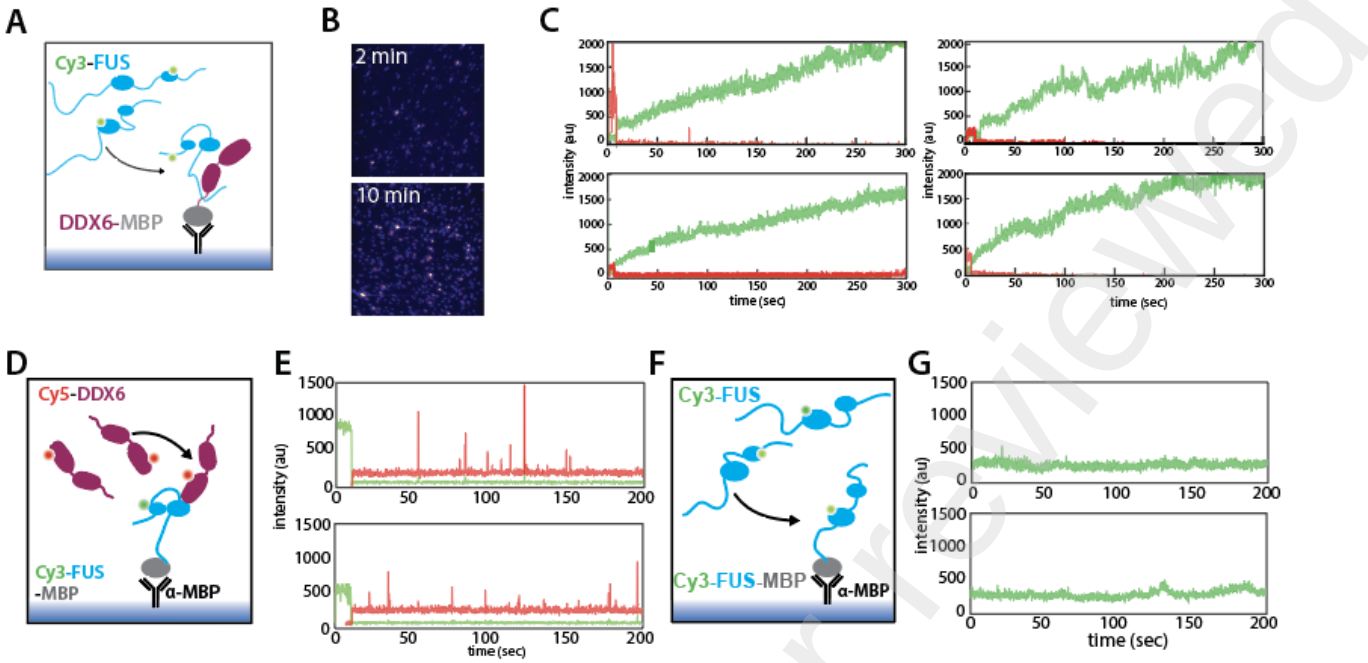

Figure 4: A single molecule of DDX6 can nucleate FUS clusters. (A) Schematic of TIRFM experimental setup with fixed DDX6-MBP (cy5) and FUS (Cy3) flowed in the imaging chamber. **(B)** Image of TIRF slide surface with Cy3/Cy5 colocalization at 2 and 10 minutes. **(C)**Representative Cy3/Cy5 TIRF traces representing linear (left) and stepwise (right) increases in Cy3 intensity. **(D)** Schematic of inverse experimental setup with fixed FUS-MBP (Cy3) and DDX6 (Cy5) flowed in. **(E)**Representative Cy3/Cy5 traces showing spikes in Cy5 intensity with no change in average intensity over time. **(F)** Schematic of experimental setup with fixed FUS-MBP (Cy3) with free FUS (Cy3) flowed in. **(G)**Representative traces Cy3 traces showing no change in intensity over time.

Figure 5

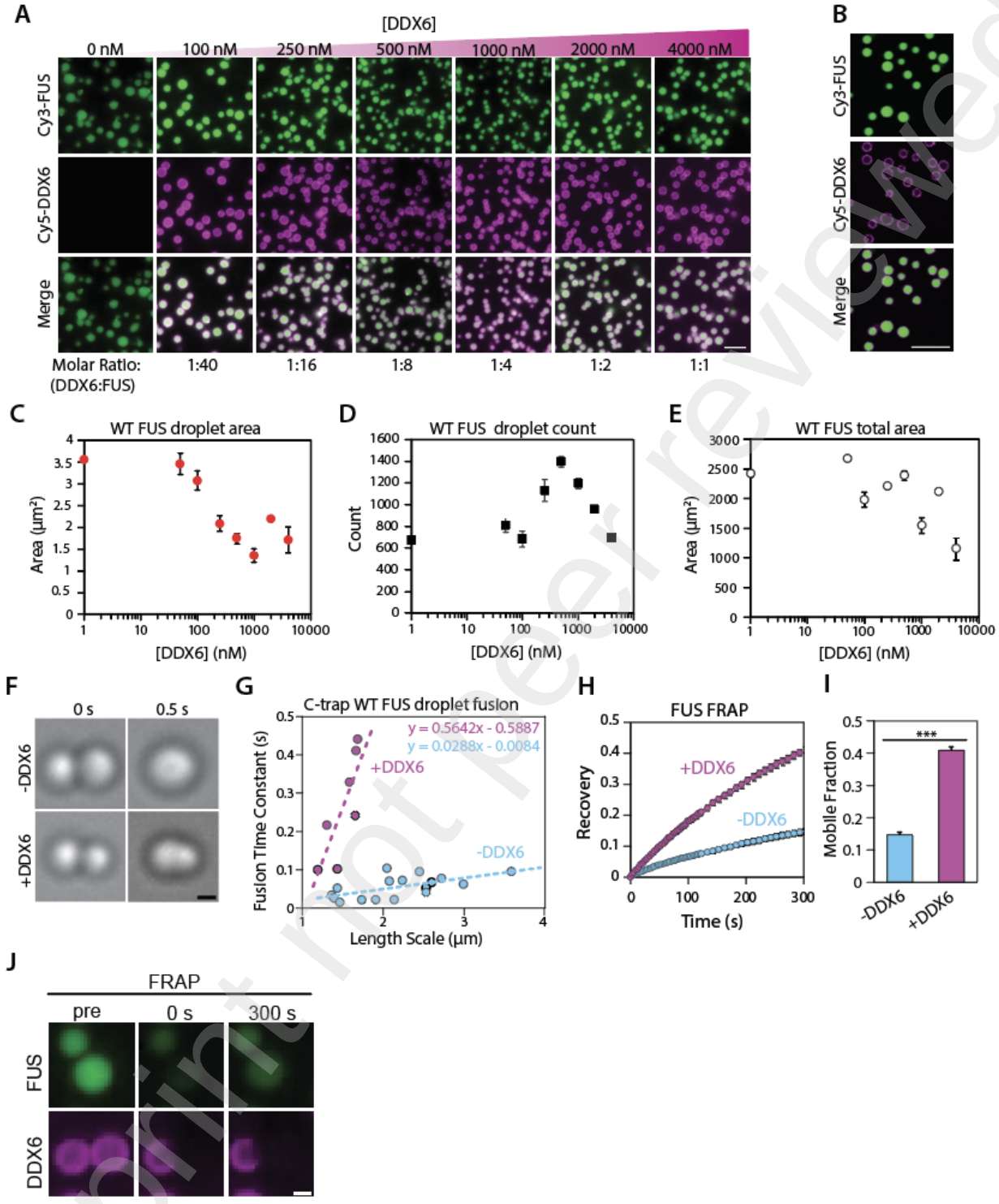

Figure 5: DDX6 regulates FUS condensate size and coarsening. (A) Representative wide-field fluorescence images of 4 µM FUS + 40 nM Cy3-FUS (green) incubated with the indicated DDX6 concentration + 10 nM Cy5-DDX6 (magenta). Scale Bar = 10 µm. **(B)** Representative airyscan confocal fluorescence images of 4 µM FUS + 40 nM Cy3-FUS and 4 µM DDX6 + 40 nM Cy5-DDX6. Scale Bar = 10 µm. **(C)** Quantification of the average FUS droplet area per field-of-view. Error bars denote standard deviation. **(D)** Same as (C) but for average FUS droplet count. **(E)** Same as (C) but for total FUS droplet area coverage. (**F**)Representative confocal bright-field images of 1 µM FUS droplets with or without 1 µM DDX6 visualized by the optical trap. Scale Bar = 1 µm. **(G)** Quantification of the droplet length scale and corresponding fusion time coefficient for FUS droplets with

(magenta) or without (blue) DDX6. **(H)** FRAP of the Cy3-FUS signal in 4 μM FUS droplets with (magenta) or without (blue) 4 μM DDX6. **(I)** Mobile fraction value for FRAP measured in (E) at 300 s. **(J)** Screen capture of Cy3-FUS (green) and Cy5-DDX6 (magenta) FRAP showing a droplet pre, at, and 300 seconds after bleaching.

Figure 6

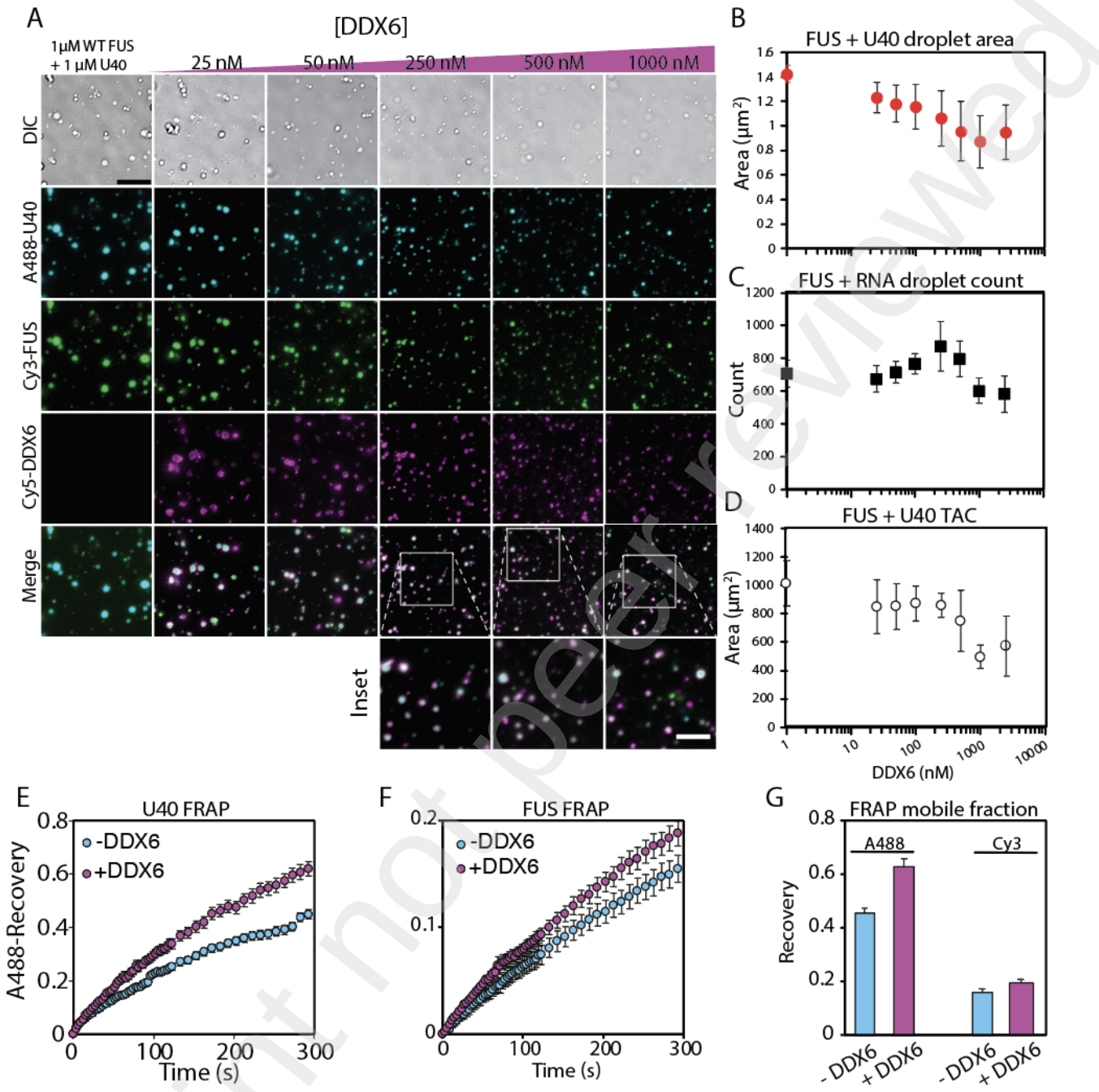

Figure 6: FUS-RNA condensates are regulated by DDX6. (A) Wide-field bright-field and fluorescence images of 1 μM FUS + 10 nM Cy3-FUS (green), 1 μM U_{40} + 10 nM A488-U_{40} (cyan), and the indicated DDX6 concentration + 10 nM Cy5-DDX6 (magenta). **(B)** Quantification of average FUS-RNA droplet count per field-of-view for increasing concentrations of DDX6. Error bars denote standard deviation. **(C)** Same as (B) but for average FUS-RNA droplet area. **(D)** Same as (B) but for average total area coverage (TAC). **(E)** Average FRAP of A488-U_{40} over time for FUS-RNA droplets with (magenta) or without (blue) DDX6. Error bars denote standard deviation. **(F)** Same as (E) but for Cy3-FUS signal. **(G)** Average FRAP value at 300 s for A488-U_{40} and Cy3-FUS with (magenta) or without (blue) DDX6. Error bars denote standard deviation

Figure 7

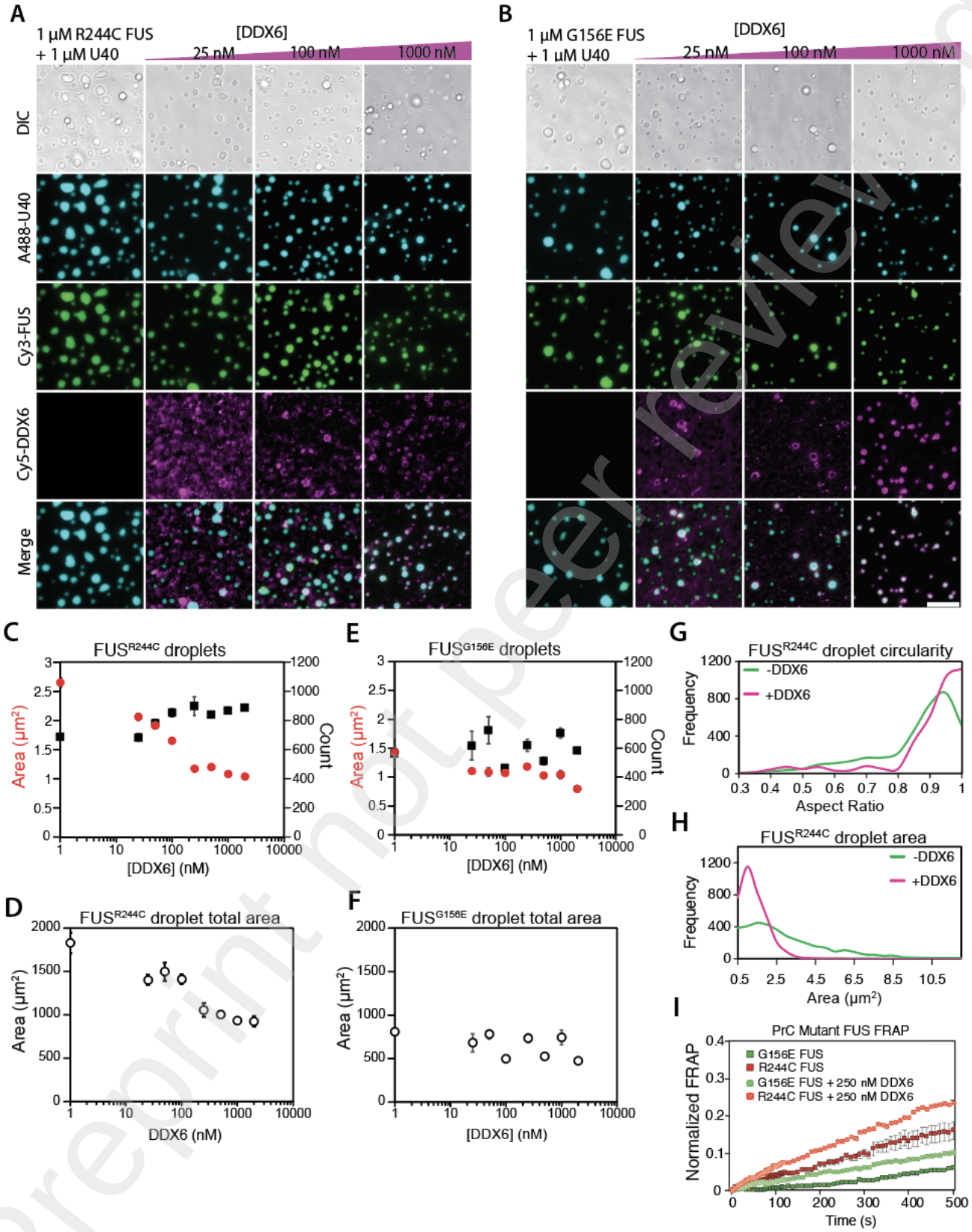

Figure 7: DDX6 antagonizes aberrant phase separation of FUS mutants. (A) Wide-field bright-field and fluorescence images of 1 μM FUS^{R244C} + 10 nM Cy3-FUS^{R244C} (green), 1 μM U_{40} + 10 nM A488-U_{40} (cyan), and the indicated DDX6 concentration + 10 nM Cy5-DDX6 (magenta). **(B)** Same as (A) but for FUS^{G156E}. **(C)**

Quantification of average FUS^{R244C} droplet area (black) and count (red) with increasing DDX6 concentrations. Error bars denote standard error. **(D)** Quantification of total area coverage of FUS^{R244C} droplets with increasing concentrations of DDX6. Error bars denote standard error. **(E)** Same as (C) but for FUS^{G156E}. **(F)** Same as (D) but for FUS^{G156E}. **(G)** Histogram plot of FUS^{R244C} droplet circularity with 1 μM DDX6 (magenta) or without DDX6 (green). **(H)** Same as (G) but for average FUS^{R244C} droplet area. **(I)** Average FRAP over time of the indicated FUS condensates with or without DDX6. Error bars denote standard error.

REFERENCE

1. Alberti, S. and A.A. Hyman, *Biomolecular condensates at the nexus of cellular stress, protein aggregation disease and ageing.* Nature reviews Molecular cell biology, 2021. **22**(3): p. 196-213.
2. Riback, J.A., et al., *Stress-triggered phase separation is an adaptive, evolutionarily tuned response.* Cell, 2017. **168**(6): p. 1028-1040. e19.
3. Yang, P., et al., *G3BP1 is a tunable switch that triggers phase separation to assemble stress granules.* Cell, 2020. **181**(2): p. 325-345. e28.
4. Yoo, H., et al., *Chaperones directly and efficiently disperse stress-triggered biomolecular condensates.* Molecular Cell, 2022. **82**(4): p. 741-755. e11.
5. Duan, Y., et al., *PARylation regulates stress granule dynamics, phase separation, and neurotoxicity of disease-related RNA-binding proteins.* Cell research, 2019. **29**(3): p. 233-247.
6. Majerciak, V., et al., *RNA helicase DDX6 and scaffold protein GW182 in P-bodies promote biogenesis of stress granules.* Nucleic Acids Res, 2023. **51**(17): p. 9337-9355.
7. Wilbertz, J.H., et al., *Single-molecule imaging of mRNA localization and regulation during the integrated stress response.* Molecular cell, 2019. **73**(5): p. 946-958. e7.
8. Frottin, F., et al., *The nucleolus functions as a phase-separated protein quality control compartment.* Science, 2019. **365**(6451): p. 342-347.
9. Lafontaine, D.L., et al., *The nucleolus as a multiphase liquid condensate.* Nature reviews Molecular cell biology, 2021. **22**(3): p. 165-182.
10. Riback, J.A., et al., *Composition-dependent thermodynamics of intracellular phase separation.* Nature, 2020. **581**(7807): p. 209-214.
11. Gwon, Y., et al., *Ubiquitination of G3BP1 mediates stress granule disassembly in a context-specific manner.* Science, 2021. **372**(6549): p. eabf6548.
12. Tripathi, V., et al., *SRSF1 regulates the assembly of pre-mRNA processing factors in nuclear speckles.* Molecular biology of the cell, 2012. **23**(18): p. 3694-3706.
13. Putnam, A., et al., *A gel phase promotes condensation of liquid P granules in Caenorhabditis elegans embryos.* Nature structural & molecular biology, 2019. **26**(3): p. 220-226.
14. Saha, S., et al., *Polar positioning of phase-separated liquid compartments in cells regulated by an mRNA competition mechanism.* Cell, 2016. **166**(6): p. 1572-1584. e16.
15. Folkmann, A.W., et al., *Regulation of biomolecular condensates by interfacial protein clusters.* Science, 2021. **373**(6560): p. 1218-1224.
16. Yao, R.-W., et al., *Nascent pre-rRNA sorting via phase separation drives the assembly of dense fibrillar components in the human nucleolus.* Molecular cell, 2019. **76**(5): p. 767-783. e11.
17. Wu, M., et al., *lncRNA SLERT controls phase separation of FC/DFCs to facilitate Pol I transcription.* Science, 2021. **373**(6554): p. 547-555.
18. Xing, Y.-H., et al., *SLERT regulates DDX21 rings associated with Pol I transcription.* Cell, 2017. **169**(4): p. 664-678. e16.
19. Rhine, K., et al., *ALS/FTLD-Linked Mutations in FUS Glycine Residues Cause Accelerated Gelation and Reduced Interactions with Wild-Type FUS.* Mol Cell, 2020. **80**(4): p. 666-681 e8.
20. Masuda, A., J.i. Takeda, and K. Ohno, *FUS-mediated regulation of alternative RNA processing in neurons: insights from global transcriptome analysis.* Wiley Interdisciplinary Reviews: RNA, 2016. **7**(3): p. 330-340.
21. Polymenidou, M., et al., *Misregulated RNA processing in amyotrophic lateral sclerosis.* Brain research, 2012. **1462**: p. 3-15.
22. Lagier-Tourenne, C., et al., *Divergent roles of ALS-linked proteins FUS/TLS and TDP-43 intersect in processing long pre-mRNAs.* Nature neuroscience, 2012. **15**(11): p. 1488-1497.
23. Murthy, A.C., et al., *Molecular interactions underlying liquid− liquid phase separation of the FUS low-complexity domain.* Nature structural & molecular biology, 2019. **26**(7): p. 637-648.

24. Baade, I., et al., *The RNA-binding protein FUS is chaperoned and imported into the nucleus by a network of import receptors.* Journal of Biological Chemistry, 2021. **296**.
25. Vance, C., et al., *Mutations in FUS, an RNA processing protein, cause familial amyotrophic lateral sclerosis type 6.* Science, 2009. **323**(5918): p. 1208-1211.
26. Portz, B., B.L. Lee, and J. Shorter, *FUS and TDP-43 phases in health and disease.* Trends in biochemical sciences, 2021. **46**(7): p. 550-563.
27. Carey, J.L. and L. Guo, *Liquid-liquid phase separation of TDP-43 and FUS in physiology and pathology of neurodegenerative diseases.* Frontiers in Molecular Biosciences, 2022. **9**: p. 826719.
28. Niaki, A.G., et al., *Loss of dynamic RNA interaction and aberrant phase separation induced by two distinct types of ALS/FTD-linked FUS mutations.* Molecular cell, 2020. **77**(1): p. 82-94. e4.
29. Szewczyk, B., et al., *FUS ALS neurons activate major stress pathways and reduce translation as an early protective mechanism against neurodegeneration.* Cell Reports, 2023. **42**(2).
30. Naumann, M., et al., *Impaired DNA damage response signaling by FUS-NLS mutations leads to neurodegeneration and FUS aggregate formation.* Nature communications, 2018. **9**(1): p. 335.
31. Hewitt, C., et al., *Novel FUS/TLS mutations and pathology in familial and sporadic amyotrophic lateral sclerosis.* Archives of neurology, 2010. **67**(4): p. 455-461.
32. Groen, E.J., et al., *FUS mutations in familial amyotrophic lateral sclerosis in the Netherlands.* Archives of neurology, 2010. **67**(2): p. 224-230.
33. Ferraiuolo, L., et al., *Molecular pathways of motor neuron injury in amyotrophic lateral sclerosis.* Nature Reviews Neurology, 2011. **7**(11): p. 616-630.
34. Deng, H., K. Gao, and J. Jankovic, *The role of FUS gene variants in neurodegenerative diseases.* Nature Reviews Neurology, 2014. **10**(6): p. 337-348.
35. Bosco, D.A., et al., *Mutant FUS proteins that cause amyotrophic lateral sclerosis incorporate into stress granules.* Human molecular genetics, 2010. **19**(21): p. 4160-4175.
36. An, H., et al., *ALS-linked cytoplasmic FUS assemblies are compositionally different from physiological stress granules and sequester hnRNPA3, a novel modifier of FUS toxicity.* Neurobiology of disease, 2022. **162**: p. 105585.
37. Reber, S., et al., *The phase separation-dependent FUS interactome reveals nuclear and cytoplasmic function of liquid–liquid phase separation.* Nucleic acids research, 2021. **49**(13): p. 7713-7731.
38. Baron, D.M., et al., *Amyotrophic lateral sclerosis-linked FUS/TLS alters stress granule assembly and dynamics.* Molecular neurodegeneration, 2013. **8**(1): p. 1-18.
39. Baron, D.M., et al., *Quantitative proteomics identifies proteins that resist translational repression and become dysregulated in ALS-FUS.* Human molecular genetics, 2019. **28**(13): p. 2143-2160.
40. Blokhuis, A.M., et al., *Comparative interactomics analysis of different ALS-associated proteins identifies converging molecular pathways.* Acta neuropathologica, 2016. **132**: p. 175-196.
41. Kamelgarn, M., et al., *Proteomic Analysis of FUS interacting proteins provides insights into FUS function and its role in ALS.* Biochimica et Biophysica Acta (BBA)-Molecular Basis of Disease, 2016. **1862**(10): p. 2004-2014.
42. Rhine, K., et al., *Poly (ADP-ribose) drives condensation of FUS via a transient interaction.* Molecular cell, 2022. **82**(5): p. 969-985. e11.
43. Paul, T. and S. Myong, *Protocol for generation and regeneration of PEG-passivated slides for single-molecule measurements.* STAR protocols, 2022. **3**(1): p. 101152.
44. Paul, T., T. Ha, and S. Myong, *Regeneration of PEG slide for multiple rounds of single-molecule measurements.* Biophysical journal, 2021. **120**(9): p. 1788-1799.
45. Rhine, K., S. Skanchy, and S. Myong, *Single-molecule and ensemble methods to probe RNP nucleation and condensate properties.* Methods, 2022. **197**: p. 74-81.
46. Rhine, K. and S. Myong, *Single molecule probing of disordered RNA binding proteins.* STAR protocols, 2022. **3**(1): p. 101131.

47. Fare, C.M., et al., *A minimal construct of nuclear-import receptor Karyopherin-β2 defines the regions critical for chaperone and disaggregation activity.* Journal of Biological Chemistry, 2023. **299**(2).
48. Guo, L., et al., *Nuclear-import receptors reverse aberrant phase transitions of RNA-binding proteins with prion-like domains.* Cell, 2018. **173**(3): p. 677-692. e20.
49. Yamazaki, T., et al., *FUS-SMN protein interactions link the motor neuron diseases ALS and SMA.* Cell reports, 2012. **2**(4): p. 799-806.
50. Deng, J., et al., *FUS interacts with ATP synthase beta subunit and induces mitochondrial unfolded protein response in cellular and animal models.* Proceedings of the National Academy of Sciences, 2018. **115**(41): p. E9678-E9686.
51. Yoshizawa, T., et al., *Nuclear import receptor inhibits phase separation of FUS through binding to multiple sites.* Cell, 2018. **173**(3): p. 693-705. e22.
52. Liu, Z., et al., *Hsp27 chaperones FUS phase separation under the modulation of stress-induced phosphorylation.* Nature structural & molecular biology, 2020. **27**(4): p. 363-372.
53. Kedersha, N., et al., *G3BP–Caprin1–USP10 complexes mediate stress granule condensation and associate with 40S subunits.* Journal of Cell Biology, 2016. **212**(7).
54. Sanders, D.W., et al., *Competing protein-RNA interaction networks control multiphase intracellular organization.* Cell, 2020. **181**(2): p. 306-324. e28.
55. Kaur, T., et al., *Sequence-encoded and composition-dependent protein-RNA interactions control multiphasic condensate morphologies.* Nature communications, 2021. **12**(1): p. 872.
56. Hochmair, J., et al., *Molecular crowding and RNA synergize to promote phase separation, microtubule interaction, and seeding of Tau condensates.* The EMBO Journal, 2022. **41**(11): p. e108882.
57. Maharana, S., et al., *RNA buffers the phase separation behavior of prion-like RNA binding proteins.* Science, 2018. **360**(6391): p. 918-921.
58. Alexander, E.J., et al., *Ubiquilin 2 modulates ALS/FTD-linked FUS–RNA complex dynamics and stress granule formation.* Proceedings of the National Academy of Sciences, 2018. **115**(49): p. E11485-E11494.
59. Fenix, A.M., et al., *Gain-of-function cardiomyopathic mutations in RBM20 rewire splicing regulation and re-distribute ribonucleoprotein granules within processing bodies.* Nature Communications, 2021. **12**(1): p. 6324.
60. Buchan, J.R., D. Muhlrad, and R. Parker, *P bodies promote stress granule assembly in Saccharomyces cerevisiae.* The Journal of cell biology, 2008. **183**(3): p. 441-455.
61. Ozgur, S., et al., *Structure of a human 4E-T/DDX6/CNOT1 complex reveals the different interplay of DDX6-binding proteins with the CCR4-NOT complex.* Cell reports, 2015. **13**(4): p. 703-711.
62. Smillie, D.A. and J. Sommerville, *RNA helicase p54 (DDX6) is a shuttling protein involved in nuclear assembly of stored mRNP particles.* J Cell Sci, 2002. **115**(Pt 2): p. 395-407.
63. Sharif, H., et al., *Structural Analysis of the yeast Dhh1–Pat1 complex reveals how Dhh1 engages Pat1, Edc3 and RNA in mutually exclusive interactions.* Nucleic Acids Research, 2013. **41**(17): p. 8377-8390.
64. Ripin, N., et al., *DDX6 modulates P-body and stress granule assembly, composition, and docking.* Journal of Cell Biology, 2024. **223**(6): p. e202306022.
65. Kelley, F.M., et al., *Amphiphilic proteins coassemble into multiphasic condensates and act as biomolecular surfactants.* Proceedings of the National Academy of Sciences, 2021. **118**(51): p. e2109967118.
66. Fei, J., et al., *Quantitative Analysis of multilayer organization of proteins and RNA in nuclear speckles at super resolution.* Journal of cell science, 2017. **130**(24): p. 4180-4192.
67. Yu, H., et al., *HSP70 chaperones RNA-free TDP-43 into anisotropic intranuclear liquid spherical shells.* Science, 2021. **371**(6529): p. eabb4309.

68. Feric, M., et al., *Coexisting liquid phases underlie nucleolar subcompartments.* Cell, 2016. **165**(7): p. 1686-1697.
69. Kamenska, A., et al., *The DDX6–4E-T interaction mediates translational repression and P-body assembly.* Nucleic acids research, 2016. **44**(13): p. 6318-6334.
70. Choksupmanee, O., et al., *Specific Interaction of DDX6 with an RNA Hairpin in the 3´ UTR of the Dengue Virus Genome Mediates G1 Phase Arrest.* Journal of Virology, 2021. **95**(17): p. 10.1128/jvi. 00510-21.
71. Mathys, H., et al., *Structural and biochemical insights to the role of the CCR4-NOT complex and DDX6 ATPase in microRNA repression.* Molecular cell, 2014. **54**(5): p. 751-765.
72. Sunde, M., C.L. Pham, and A.H. Kwan, *Molecular characteristics and biological functions of surface-active and surfactant proteins.* Annual review of biochemistry, 2017. **86**: p. 585-608.
73. Kar, M., et al., *Phase-separating RNA-binding proteins form heterogeneous distributions of clusters in subsaturated solutions.* Proceedings of the National Academy of Sciences, 2022. **119**(28): p. e2202222119.
74. Ray, S., et al., *Mass photometric detection and quantification of nanoscale α-synuclein phase separation.* Nature Chemistry, 2023: p. 1-11.
75. Cardona, A.H., et al., *Self-demixing of mRNA copies buffers mRNA: mRNA and mRNA: regulator stoichiometries.* Cell, 2023. **186**(20): p. 4310-4324. e23.
76. Hondele, M., et al., *DEAD-box ATPases are global regulators of phase-separated organelles.* Nature, 2019. **573**(7772): p. 144-148.
77. Weber, R. and C.-T. Chang, *Human DDX6 regulates translation and decay of inefficiently translated mRNAs.* Elife, 2024. **13**: p. RP92426.
78. Fagerberg, L., et al., *Analysis of the human tissue-specific expression by genome-wide integration of transcriptomics and antibody-based proteomics.* Molecular & cellular proteomics, 2014. **13**(2): p. 397-406.
79. Ayache, J., et al., *P-body assembly requires DDX6 repression complexes rather than decay or Ataxin2/2L complexes.* Molecular Biology of the Cell, 2015. **26**(14): p. 2579-2595.